

# Piecewise potential vorticity diagnosis of the development of a polar low over the Sea of Japan

By LONGTAO WU\*, JONATHAN E. MARTIN and GRANT W. PETTY, *Department of Atmospheric and Oceanic Sciences University of Wisconsin-Madison, Madison, WI 53706, USA*

(Manuscript received 6 July 2010; in final form 22 December 2010)

## ABSTRACT

The piecewise potential vorticity (PV) inversion method developed by Davis and Emanuel (1991) is used to diagnose the development processes of a polar low over the Sea of Japan in December 2003. The synoptic scale-balanced flows associated with the polar low are successfully captured using the inversion method. It is shown that, antecedent to the development of the polar low, a positive lower-tropospheric temperature anomaly was induced by the approach of a positive tropopause-level PV anomaly over the northern Sea of Japan. The analysis suggests that the polar low was initiated as a result of the combined effect of the positive PV anomaly near the tropopause and the near-surface positive temperature anomaly. The rapid height falls in the lower troposphere were primarily contributed by the upper tropospheric PV anomaly. Further intensification of the polar low was afforded by latent heat release associated with cloud and precipitation processes. After the polar low moved over northern Honshu, quick dissipation was primarily rendered by the thinning and elongating of the upper level PV anomaly that led to a rapid reduction of the lower troposphere height perturbations associated with it.

## 1. Introduction

Polar lows (Rasmussen and Turner, 2003) are intense mesoscale cyclones that often develop over the subpolar oceans and exhibit lifecycles ranging from hours to days. These storms are most often manifest in comma and spiraliform cloud patterns as viewed in satellite imagery and are regarded as difficult to forecast as a result of their relatively small scales and short lifecycles.

In the early days of polar low research, considerable debate existed concerning whether polar lows were purely baroclinic systems (Harrold and Browning, 1969; Mansfield, 1974) or were dominated by deep convection (Rasmussen, 1979). It is now widely accepted that baroclinic conversion and air–sea interaction, which spawns deep convection, are the two primary energetic mechanisms driving polar low formation (Rasmussen and Turner, 2003).

Since the 1990s, observational case studies and numerical simulations of polar lows (Nordeng and Rasmussen, 1992; Rasmussen et al., 1992; Grønås and Kvamstø, 1995; Guo et al., 2007) suggest that the development of polar lows, though usually initiated by upper-level potential vorticity (PV) anomalies interacting with strong surface baroclinicity, is greatly enhanced

by the presence of deep moist convection and strong fluxes of latent and sensible heat from the ocean (Grønås and Kvamstø, 1995; Bresch et al., 1997; Yanase et al., 2004; Guo et al., 2007). Montgomery and Farrell (1992) proposed a two stage development model. In the first stage, the combined effect of an upper-level PV anomaly and a low-level baroclinic zone induces a self-development process in which rapid low-level spin up and generation of low- and midlevel PV anomalies augment the baroclinic interaction between these systems. In the second stage, the latent heating associated with the development of clouds and precipitation intensifies the polar low development by enhancing the upward motion. This model suggests that polar low development is broadly similar to mid-latitude cyclonic development, albeit with moist processes characteristically playing a more substantial role in the intensification of polar lows.

In the real atmosphere, the relative importance of the various developmental processes varies from case to case and changes during the lifecycle. In order to develop a complete understanding of the dynamics of a polar low, the relative importance of each process must be discerned. Sensitivity studies, in which certain physical processes are switched on or off in a suite of numerical model simulations, have commonly been used to investigate the importance of various processes on polar low development (e.g. Bresch et al., 1997; Yanase et al., 2004; Guo et al., 2007). Since the effect of one physical process is often coupled to the

\*Corresponding author.

e-mail: Longtao.Wu@jpl.nasa.gov

DOI: 10.1111/j.1600-0870.2011.00511.x

others, artificial removal of one can affect the model atmosphere in unanticipated ways. This non-linearity of physical interactions imposes an inherent limitation on the insights gained by such sensitivity studies.

An alternative method by which to investigate the relative importance of various physical processes on the development of polar lows involves piecewise PV inversion (Hoskins et al., 1985; Davis and Emanuel, 1991; Bracegirdle et al., 2009). Two properties of PV, conservation and invertibility, make it a useful diagnostic quantity for the study of nearly balanced atmospheric flows. In adiabatic, inviscid flow, PV is conserved under the full primitive equations for the complete atmospheric system. The invertibility principle states that given a distribution of PV, a balance condition relating the mass and momentum fields, and boundary conditions on the analysis domain, there is only one set of balanced wind and temperature fields associated with a particular PV distribution. Additional insights into cyclone dynamics can be obtained by considering the non-conservation of PV (Stoelinga, 1996), which states that their PV distribution can be changed by adding new PV anomalies as a result of diabatic heating or friction.

The non-linear piecewise PV inversion method developed by Davis and Emanuel (1991, hereafter DE) allows recovery of the subset of the wind and temperature fields attributable to a discrete PV anomaly. Thus, the effect of a discrete PV anomaly during the development of a weather system can be clearly revealed from the piecewise PV inversion results. Accordingly, the relative importance of discrete PV anomalies on the development of a given weather system can also be deduced. The DE method has been primarily used to understand the nature of extratropical cyclones and the role of latent heat release (LHR) in cyclone evolution (e.g. Davis and Emanuel, 1991; Davis et al., 1993; Stoelinga, 1996; Korner and Martin, 2000; Martin and Marsili, 2002; Martin and Otkin, 2004; Posselt and Martin, 2004).

Although some fraction of the total circulation associated with a polar low is likely unbalanced, Rasmussen and Turner (2003) suggest that considerable insight into the dynamical nature of these storms can be obtained by considering their 'balanced dynamics'. Bracegirdle and Gray (2009) implemented a piecewise PV inversion method to assess the relative importance of different PV anomalies and their interaction during a polar low over Norwegian Sea on 13 October 1993. It was shown that the polar low was initiated by a positive upper-level PV anomaly. After that, the intensification of the polar low was dominated by the lower troposphere PV anomaly associated with LHR, consistent with nearly all prior studies of polar lows. Their analysis revealed that a third stage of development, dominated by wind-induced surface heat exchange, might be a reasonable addition to the two stage development of polar lows proposed by Montgomery and Farrell (1992).

In this paper, the lifecycle of a polar low that developed over the Sea of Japan in December 2003 is investigated. Output from a numerical simulation of the storm undertaken using the Weather

Research and Forecasting (WRF) model is used to perform a piecewise PV inversion in order to examine the relative influences of upper tropospheric, lower tropospheric and diabatic PV anomalies in the development of the polar low. Unlike most other polar lows described in the literature, the analysis will reveal that the life cycle of this storm was shaped primarily by the influence of the upper-level PV anomaly with LHR playing a subordinate role. The paper is structured as follows. In Section 2, a synoptic description of the case is provided using analysis from the NCEP FNL data set. Section 3 contains the description of model setups and the evaluation of model outputs. Section 4 describes the piecewise PV inversion procedure and presents results from the analyses. A summary and conclusion are offered in Section 5.

## 2. Synoptic overview

At 0600 UTC 19 December 2003, an extratropical cyclone of modest intensity (labelled A in Fig. 1a) was beginning to form just east of Japan downstream of a broad 500 hPa trough centred over the western Sea of Japan. A surface trough (labelled P in Fig. 1a), which later developed into polar low P, was seen just west of Hokkaido, in proximity to a local ridge in the 1000–500 hPa thickness field (Fig. 1a). The confluent flow associated with this trough advected warm, moist marine air toward cold, dry continental air to the northwest. The 500 hPa trough contained two vorticity maxima, one (labelled S in Fig. 1b) associated with cyclone A, and the other (labelled N in Fig. 1b) associated with the surface trough. The vorticity maximum N (S) was just upshear of the development region of the polar low P (cyclone A), consistent with the relationship of cyclonic vorticity advection by the thermal wind to upward vertical motion as described by Sutcliffe (1947) and Trenberth (1978). At 350 hPa a dipole PV structure was evident with the eastern maximum associated with cyclone A while the more intense western maximum was centred over the Sea of Japan (Fig. 1c).

By 1800 UTC 19 December, cyclone A had deepened rapidly to a minimum sea level pressure (SLP) of 980 hPa (Fig. 2a). The surface trough originally west of Hokkaido had moved slightly southward, intensified somewhat, and was characterized by a strong pressure gradient to its northwest by this time (Fig. 2a). The development of this feature in the SLP field was accompanied by an intensification of its associated 1000–500 hPa thickness ridge as well. The polar low was the emerging feature in this developing trough. The 500 hPa trough had weakened somewhat while another short-wave had developed to the northeast of the geopotential height minimum. The vorticity maximum S moved eastward and covered a larger region (Fig. 2b). The vorticity maximum N, meanwhile, moved southeastward and had intensified by this time. The 350-hPa PV feature moved southeastward while deepening slightly and becoming zonally elongated (Fig. 2c).

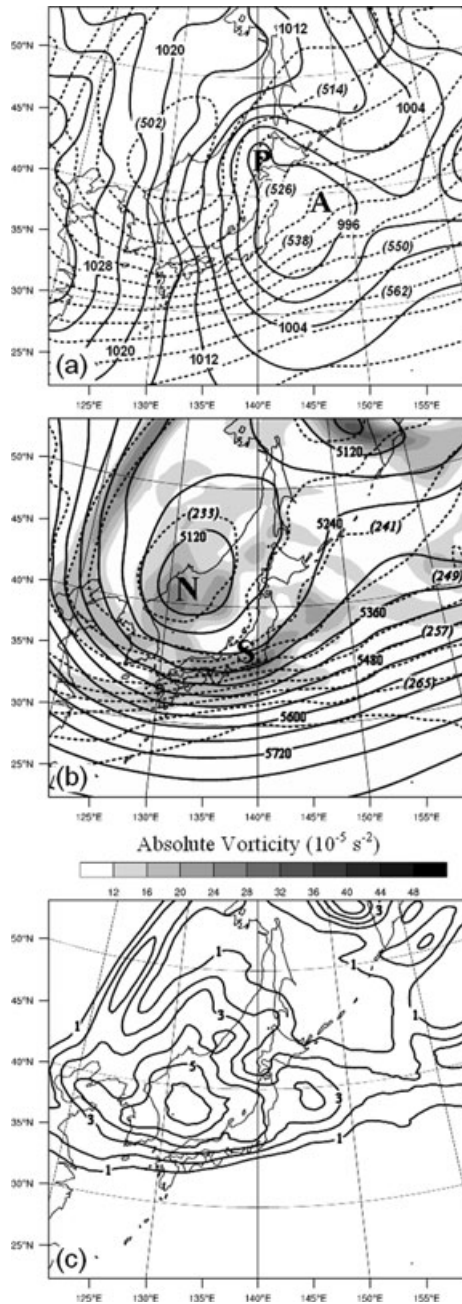


*Fig. 1.* NCEP FNL analyses data at 0600 UTC 19 December 2003. (a) SLP (solid lines, contoured at 4 hPa intervals) and 1000–500 hPa thickness (dashed lines, unit: 10 m, contoured at 60 m intervals); Symbol 'A' and 'P' represent the centre of extratropical cyclone A and polar low P, respectively. (b) The 500 hPa geopotential height (solid lines, contoured at 60 m intervals), temperature (dashed lines, contoured at 4 K intervals) and absolute vorticity (shaded); Symbol 'N' and 'S' represent the positions of the two vorticity maxima, respectively. (c) The 350 hPa PV; PV is labelled in PVU ( $1 \text{ PVU} = 10^{-6} \text{ m}^2 \text{ K kg}^{-1} \text{ s}^{-1}$ ) and contoured by every 1 PVU beginning at 1 PVU.

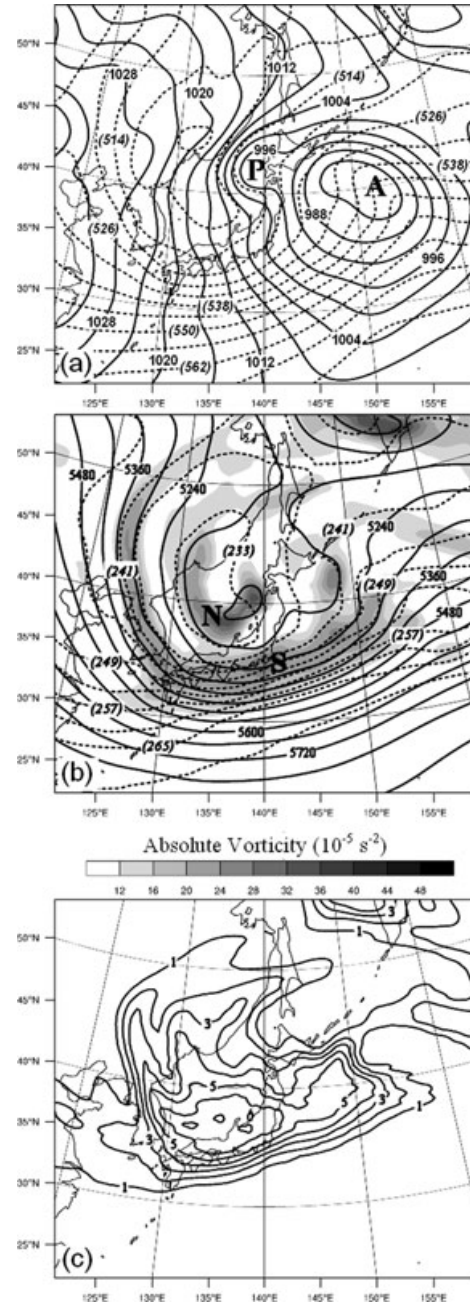


*Fig. 2.* NCEP FNL analyses data at 1800 UTC 19 December 2003. (a) As for Fig. 1a. (b) As for Fig. 1b. (c) As for Fig. 1c.

Over the next 6 h, cyclone A continued developing (Fig. 3a). A rapid development of the polar low also occurred during this time period. By 0000 UTC 20 December, a closed low with a minimum SLP of 993 hPa had developed in association with the polar low (Fig. 3a) as it continued its southeastward movement. The trough at 500 hPa continued to weaken while the

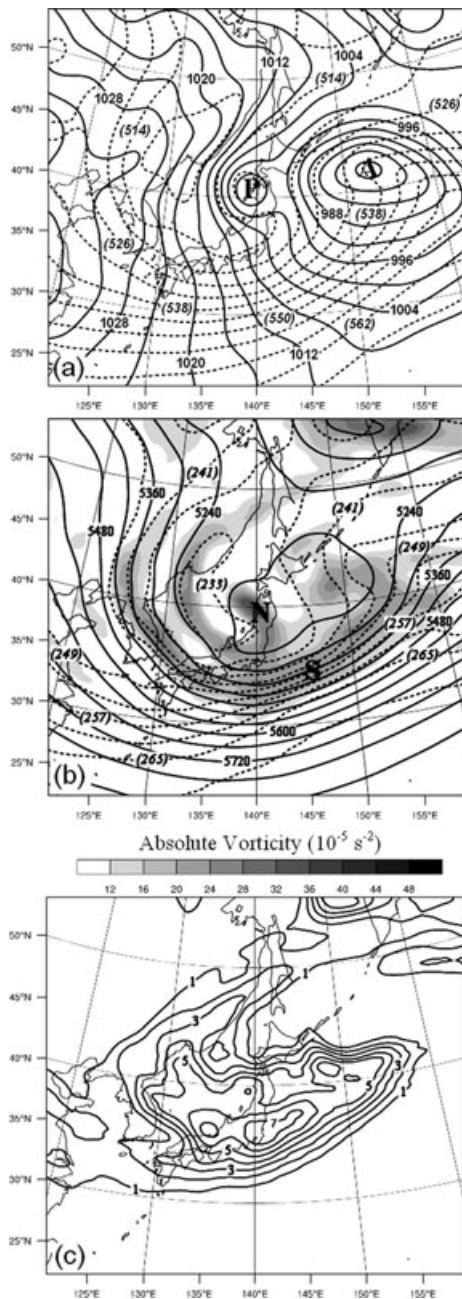


Fig. 3. NCEP FNL analyses data at 0000 UTC 20 December 2003. (a) As for Fig. 1a. (b) As for Fig. 1b. (c) As for Fig. 1c.

vorticity maximum N began to merge with the vorticity maximum S (Fig. 3b). The PV feature at 350 hPa continued its southeastward movement, intensified by about 1 PVU ( $1 \text{ PVU} = 10^{-6} \text{ m}^2 \text{ kg}^{-1} \text{ s}^{-1}$ ) and continued to be stretched in the zonal direction (Fig. 3c). The Geostationary Operational Environmental Satellite (GOES)-9 infrared (IR) image illustrates that a spiraliform polar low was fully developed with a clear eye at the centre by 0000 UTC 20 December (Fig. 4a). By 0600 UTC 20

December, the polar low had moved over land and quickly dissipated while the 350 hPa PV became more anisotropic through continued zonal stretching (not shown).

### 3. Model description

The WRF model is a state-of-the-art mesoscale weather prediction system. It integrates the non-hydrostatic (with a run-time hydrostatic option available), compressible dynamic equations on an Arakawa C-grid using a terrain-following hydrostatic pressure vertical coordinate. The Advanced Research WRF modelling system Version 3 was used in this study. Simulations were run with two nested domains, at 25 km and 5 km horizontal grid resolution, respectively, and with 28 eta levels in the vertical. Although the foregoing analysis relies on output from the 25 km simulation, the 5 km simulation was employed to better reproduce the synoptic environment through a two-way nesting procedure, which was used to drive WRF. The initialization fields and boundary conditions were obtained from the  $1^\circ \times 1^\circ$  National Center for Environmental Prediction final (NCEP FNL) Global Tropospheric Analyses (<http://dss.ucar.edu/datasets/ds083.2/>). The domains are shown in Fig. 5. The simulation was initialized at 1800 UTC 18 December 2003 and run for 42 h.

The principal physical schemes used in the simulations include the Yonsei University planetary boundary layer scheme (Hong et al., 2006), the Rapid Radiative Transfer Model (RRTM) long-wave scheme (Mlawer et al., 1997) and the Dudhia (1989) short-wave scheme. A modified version of the Kain–Fritsch cumulus parameterization scheme (Kain and Fritsch, 1990, 1993) was used in the outer domain, while no cumulus scheme was used in the inner domain as suggested by the WRF technical note (Skamarock et al., 2008). Wu and Petty (2010) show that the WRF Single-Moment 6-class (WSM6; Hong and Lim, 2006; Dudhia et al., 2008) microphysics scheme exhibited fewer apparent artefacts or unrealistic hydrometeor fields than any of the other four mixed-phase microphysics schemes provided with the WRF model. The WSM6 scheme was therefore used in this study.

Although a systematic evaluation of the simulation will not be offered here, the 6 hourly positions of the centres (SLP minima) of cyclone A and the polar low are shown in Fig. 5 as part of a limited evaluation of the WRF simulation. The corresponding SLPs at each time are listed in Table 1. Cyclone A is identified from 1800 UTC 18 December to 1200 UTC 20 December while the polar low is first identified at 0600 UTC 19 December when the weak trough, which later developed into the polar low, started to appear in the SLP field. The last indicated position of the polar low is at 0600 UTC 20 December. It can be seen that the WRF simulation reasonably reproduced the development of cyclone A and the polar low. The simulation successfully captured the movement of cyclone A although the difference of the positions between the FNL analyses and the WRF simulations is relatively large from 1800 UTC 19 December to 0000 UTC 20 December.

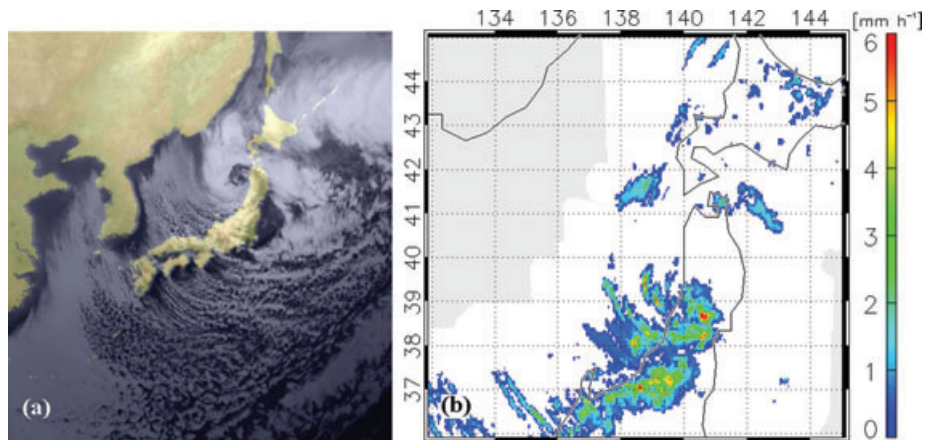


Fig. 4. (a) GOES-9 IR imagery at 0000 UTC 20 December 2003 shows a spiraliform polar low over Japan, with clear eye in the centre. (b) The precipitation rate from the Automatic Meteorological Data Acquisition System (AMeDAS) radar product at 0350 UTC 20 Dec 2003.

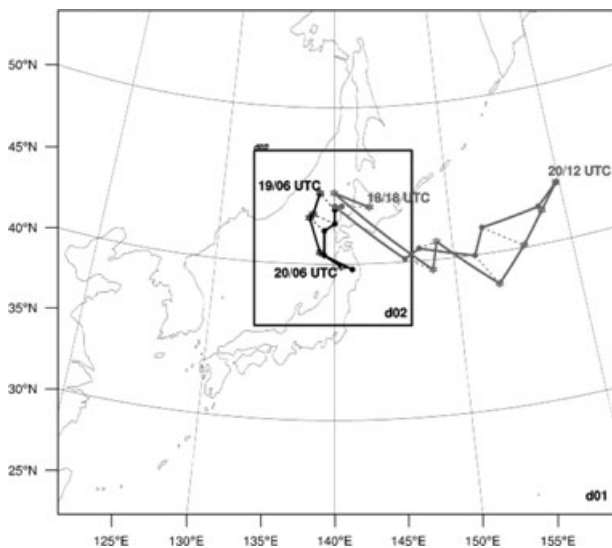


Fig. 5. Inner (d02) and outer (d01) domains of the WRF simulation used in this analysis. The centres of cyclone A and the polar low P at the sea level are also shown in the domain. Cyclone A in grey; polar low P in black; simulated data shown with star symbol; FNL analysed data shown with dot symbol. All the positions are identified at 6-h intervals according to the FNL analyses and the 25-km WRF simulations. Cyclone A is identified from 1800 UTC 18 December to 1200 UTC 20 December while the polar low P is from 0600 UTC 19 December to 0600 UTC 20 December. The time series of the same data set are connected by solid lines. At each time, the centres of the FNL analysis and WRF simulation are connected by dotted lines.

The movement of the polar low is also reasonably reproduced although the simulated initial position is a little northwest of the FNL analyses. The WRF simulations show the same trend of the SLP minima as compared to the FNL analyses for both cyclone A and the polar low (Table 1). However, more intense cyclones are shown in the simulations; maximum 11 hPa deeper for cyclone A and maximum 12 hPa deeper for the polar low.

Table 1. The FNL analysed and WRF simulated SLPs in the centre of cyclone A and the polar low P at each time.

Time	SLP (hPa) in the centre of cyclone A		SLP (hPa) in the centre of the polar low	
	FNL	WRF	FNL	WRF
1800 UTC 18 December	1001	999		
0000 UTC 19 December	999	998		
0600 UTC 19 December	992	994	995	992
1200 UTC 19 December	989	988	994	985
1800 UTC 19 December	981	978	993	983
0000 UTC 20 December	975	969	993	984
0600 UTC 20 December	972	962	996	984
1200 UTC 20 December	973	962		

Considering the coarse resolution of the FNL analyses and the fact that observational data over the ocean are sparse, it is not surprising that the FNL analyses underestimate the intensity of the lows, especially the mesoscale polar low. In addition, since both 25 km and 5 km grid spacings are inadequate to explicitly resolve convection, the grid-scale latent heating and its effect on the development, may be overestimated in the WRF simulation (Deng et al., 2004). Although the central SLP minima are different, the vortex structures are similar between the FNL analyses and the simulations after comparing the 10-m wind vectors in the vicinity of the polar low (not shown).

The polar low case in this study is also used in Wu and Petty (2010) to investigate the performance of different microphysics schemes in the simulations of polar lows. In order to better examine the whole synoptic environment affecting the development of the polar low, the simulated domain in this study is larger than that in Wu and Petty (2010). However, the results of the two simulations are consistent. Evaluation of the WRF simulation of this case was discussed in detail in Wu and Petty (2010). It was

shown that the simulation reasonably reproduced the dynamical evolution of the polar low although the simulation developed a closed low earlier than in the FNL analyses and with a lower minimum SLP.

Overall, the WRF model fairly accurately reproduced the synoptic-scale environment within which the polar low developed despite some differences between the FNL analyses and the simulations. We therefore confidently employ output from the simulation to perform the piecewise PV diagnosis of this polar low.

## 4. Piecewise PV analysis

### 4.1. Definition and inversion procedure

The Ertel potential vorticity (EPV; Rossby, 1940; Ertel, 1942) is defined as

$$EPV = \frac{1}{\rho} \boldsymbol{\eta} \cdot \nabla \theta, \quad (1)$$

where  $\rho$  is the density,  $\boldsymbol{\eta}$  is the absolute vorticity vector and  $\theta$  is the potential temperature. The conservation of EPV is not dependent on any scaling assumption. In fact, a high-order balance approximation can be used for the inversion of EPV even in situations where the Rossby number is not small (Davis and Emanuel, 1991). The Davis and Emanuel (1991) (DE) method is used in this study to investigate the processes that contributed to the development of the polar low. The Charney (1955) balance condition, which retains accuracy in highly curved flows, is used in the DE method for inversion of the full EPV. Assuming, (1) hydrostatic balance and (2) that the magnitude of the irrotational component of the wind is much smaller than the magnitude of the non-divergent component (i.e.  $|\mathbf{V}_\chi| \ll |\mathbf{V}_\psi|$ ), the divergence equation and (1) can be rewritten as

$$\nabla^2 \Phi = \nabla \cdot (f \nabla \psi) + \frac{2}{a^4 \cos^2 \phi} \frac{\partial}{\partial (\lambda, \phi)} \left( \frac{\partial \psi}{\partial \lambda}, \frac{\partial \psi}{\partial \phi} \right). \quad (2)$$

$$EPV = \frac{g\kappa\pi}{P} \left[ (f + \nabla^2 \psi) \frac{\partial^2 \Phi}{\partial \pi^2} - \frac{1}{a^2 \cos^2 \phi} \frac{\partial^2 \psi}{\partial \lambda \partial \pi} \frac{\partial^2 \Phi}{\partial \lambda \partial \pi} - \frac{1}{a^2} \frac{\partial^2 \psi}{\partial \phi \partial \pi} \frac{\partial^2 \Phi}{\partial \phi \partial \pi} \right], \quad (3)$$

where  $\Phi$  is the geopotential,  $\psi$  is the non-divergent streamfunction,  $\lambda$  is the longitude,  $\phi$  is the latitude,  $a$  is the radius of the earth,  $\kappa = R/c_p$ ,  $P$  is the pressure and  $\pi = [c_p(P/P_0)^\kappa]$  is the Exner function, which serves as the vertical coordinate.

In order to improve convergence, output from the model simulation at 25 km resolution was coarsened to  $\sim 100$  km resolution and then interpolated to 20 isobaric levels at 50-hPa intervals from 1000 hPa to 50 hPa. Since small-scale features are naturally smoothed by the inversion process (Davis et al., 1993) and our analyses focus on the environmental influences on the

polar low development, the coarsening of the grids facilitates computation without compromising the quantitative nature of the inversion results.

The PV fields are calculated from the model's wind and temperature fields at all vertical levels over grid 1. The potential temperature at 975 hPa and 75 hPa (linearly interpolated between 1000 and 950 hPa and 50 and 100 hPa, respectively) provides the Neumann boundary conditions on the horizontal boundaries. To insure convergence of the iterative method used to invert the PV, negative values of PV are set to a small positive constant value (0.01 PVU). Given these distributions of PV, a balance condition and boundary conditions, a full inversion is performed to solve for the geopotential,  $\Phi$  and the non-divergent streamfunction,  $\psi$ , associated with the total PV fields. Details of the numerical methods and boundary conditions appear in DE.

A piecewise PV inversion method is also presented in DE in order to recover the flow fields associated with discrete PV anomalies. Here the perturbation field, which is necessary for performing a piecewise PV inversion, is defined as a departure from a time mean field. The time mean field is computed from three-consecutive 42-h simulations; one initialized at 0000 UTC 17 December 2003, one initialized at 1800 UTC 18 December (the object run described in Section 3), and the other initialized at 1200 UTC 20 December 2003. The time mean is then subtracted from the instantaneous PV distribution at each discrete time in the object run to get the perturbation fields.

As the two stage development model (Montgomery and Farrell, 1992) and other studies (Nordeng and Rasmussen, 1992; Rasmussen et al., 1992; Grønås and Kvamstø, 1995; Guo et al., 2007) suggest, three important physical factors contributing to the development of polar lows are an upper-level PV anomaly, a low-level baroclinic zone and LHR. Consequently, a conventional three-way partitioning of the perturbation PV field (Korner and Martin, 2000; Martin and Marsili, 2002; Martin and Otkin, 2004) is used here in order to quantify the relative importance of these three physical factors. The total perturbation PV field is partitioned into an upper layer, an interior layer and a surface layer. The upper layer extends from 650 hPa to 50 hPa and is designed to isolate PV anomalies near the tropopause. Careful comparison between the fields of relative humidity (RH) and perturbation PV revealed that PV associated with stratospheric anomalies resided solely in air with less than 70% RH. Thus, the positive perturbation PV in this layer is set to 0.0 PVU whenever the RH is greater than 70%. The interior layer extends from 950 hPa to 400 hPa and is intended to isolate mid-troposphere PV anomalies, including the PV anomaly associated with LHR. Such anomalies were located in regions where the  $RH \geq 70\%$ . In order to guard against the scheme mistaking extruded stratospheric perturbation PV for that associated with LHR, the PV in this layer is set to 0.0 PVU whenever the RH is less than 70%. The surface layer extends from 950 to 900 hPa and also includes the 975-hPa potential temperature. This layer is designed to isolate the boundary potential temperature anomalies that are

equivalent to PV anomalies just above the surface (Bretherton, 1966). The surface layer, however, also includes perturbation PV in the 950–900 hPa layer. To ensure against redundancy with the interior layer, surface layer perturbation PV from 950 hPa to 900 hPa is set to 0.0 PVU whenever the RH is greater than 70%.

The combination of these three layers and their respective RH criteria excludes only two parts of the total perturbation PV distribution from being inverted; namely, (1) positive perturbation PV in air with RH greater than 70% in the 350–50 hPa layer, and (2) perturbation PV in air with RH less than 70% in the 850–600 hPa layer. Careful scrutiny of the data, however, revealed that these portions of the total perturbation PV distributions were very small in the present case. For the remainder of the paper,  $U_{\text{pert}}$  will refer to the PV perturbations associated with the upper layer,  $M_{\text{pert}}$  to perturbations associated with the interior layer and  $L_{\text{pert}}$  to perturbations associated with the surface layer.

#### 4.2. Evaluation of inversion results

Once the inversion is performed, the effect of each of the three pieces of the perturbation PV on the lower-tropospheric height changes during the lifecycle of the polar low is considered. Since the lowest available isobaric surface in the inversion output was 950 hPa, subsequent analysis will concentrate on the evolution of geopotential height at that level.

Figure 6 compares the 950 hPa geopotential height between the simulation and full inversion field at 0000 UTC 20 December. The full inversion field (Fig. 6b) captures a geopotential height pattern similar to that produced in the simulation field (Fig. 6a), with three low centres shown in both the model and full inversion fields. Figure 6c shows the difference in the geopotential heights between the full inversion and model height fields. The difference is small in most of the region, including where the polar low is located (Fig. 6c). As expected, relatively large differences are shown in the vicinity of the upper-level trough axis where the balance condition is most likely to be violated. Figure 7 is a time series of geopotential heights at the centre of the polar low. Note that the full inversion height agrees well with the model heights at most of the forecast times. In addition, the full inversion and the sum of the partitioned PV pieces are generally within one dam of each other, indicating that the piecewise partitioning scheme accounts for most parts of the total perturbation PV and associated perturbation heights. Given these similarities, we confidently employ the results of the piecewise PV inversion to diagnose the development of the polar low.

#### 4.3. Partitioned height changes

Figure 8 shows the 950 hPa height perturbation associated with the  $U_{\text{pert}}$  PV anomaly at 12-h intervals from 1800 UTC 18 December to 0600 UTC 20 December. The position of the 950 hPa polar low centre from the full inversion is indicated by the

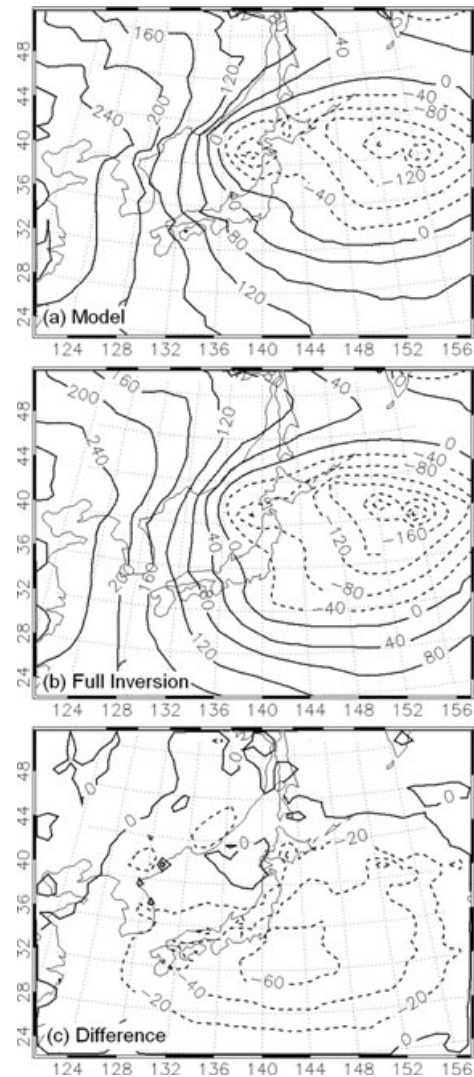


Fig. 6. (a) The WRF 950-hPa geopotential height contoured every 40 m. (b) The full inverted geopotential height contoured every 40 m. (c) The difference between the full inverted field and WRF field contoured every 20 m. All the fields are valid at 0000 UTC 20 December 2003.

star symbol for times at which the polar low centre is clearly identified. At 1800 UTC 18 December (Fig. 8a), the centre of the  $U_{\text{pert}}$  PV anomaly was located over the Eurasian continent with a minimum height perturbation of  $-119$  m at 950 hPa. A negative height perturbation (of about  $-40$  m) contributed by the  $U_{\text{pert}}$  PV anomaly was seen over the northern Sea of Japan, where the polar low later developed. At 0600 UTC 19 December (Fig. 8b), the minimum height perturbation associated with the  $U_{\text{pert}}$  PV anomaly was just moving off the Eurasian continent. A significant deepening of its associated height perturbation was seen during the 12-h period as the minimum height perturbation deepened by about 100 m. The polar low centre was located to the northeast of the minimum height perturbation associated

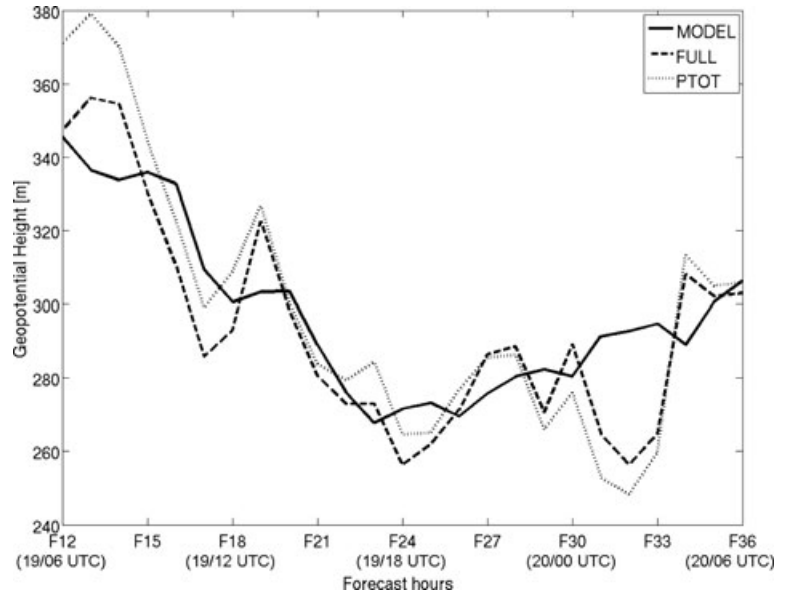


Fig. 7. Time series of geopotential heights at the centre of the polar low: WRF simulation (solid line), full inversion (dashed line) and summation of piecewise PV inversion (dotted line).

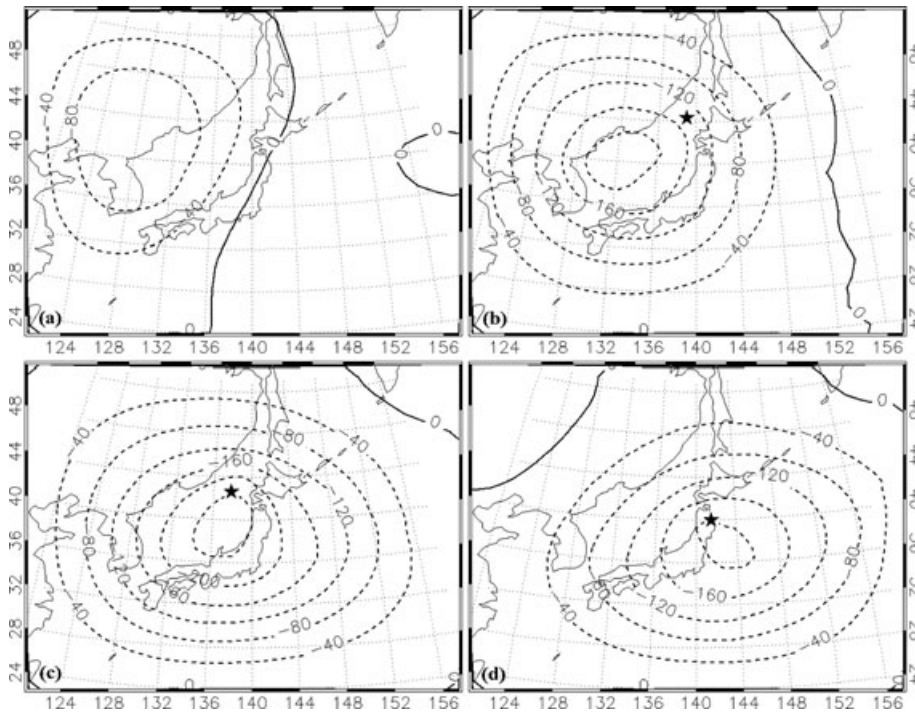


Fig. 8. The 950-hPa geopotential height perturbation associated with the  $U_{\text{pert}}$  PV anomaly. Negative (positive) geopotential height perturbations are indicated by dashed (solid) lines contoured every 40 m. The star indicates the location of the polar low centre at each time. Valid at (a) 1800 UTC 18 December; (b) 0600 UTC 19 December; (c) 1800 UTC 19 December; (d) 0600 UTC 20 December.

with the  $U_{\text{pert}}$  PV anomaly. In the next 12-h period (Fig. 8c), the height perturbation continued to deepen. The polar low centre was just north of, and closer to, the minimum height perturbation associated with the  $U_{\text{pert}}$  PV anomaly. By 0600 UTC 20 December (Fig. 8d), the height perturbation associated with the  $U_{\text{pert}}$  PV anomaly had weakened while moving to the southeast of the polar low centre.

Given that  $M_{\text{pert}}$  includes perturbation PV from 950 to 400 hPa in air with RH 70%, some synoptic-scale negative perturbation PV, in regions of cold air advection over or near the ocean, are included in  $M_{\text{pert}}$ . Consequently, weak positive height perturbations associated with the  $M_{\text{pert}}$  PV anomaly were seen over the Sea of Japan at 1800 UTC 18 December (Fig. 9a). At the same time, a weak negative height perturbation, collocated with the

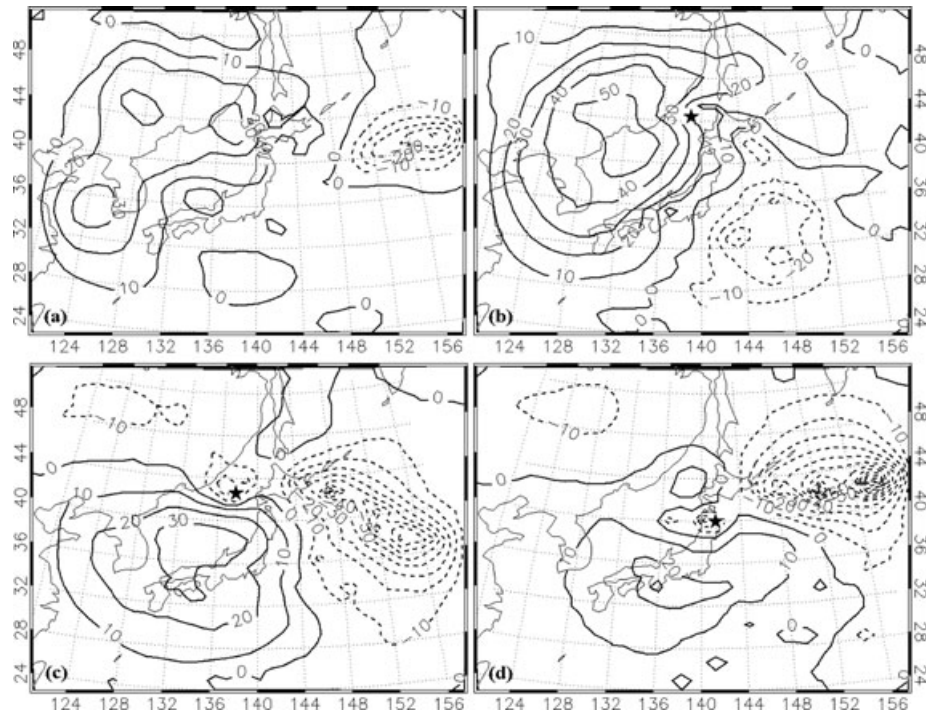


Fig. 9. The 950-hPa geopotential height perturbation associated with the  $M_{\text{pert}}$  PV anomaly. Negative (positive) geopotential height perturbations are indicated by dashed (solid) lines contoured every 10 m. The star indicates the location of the polar low centre at each time. Valid at (a) 1800 UTC 18 December; (b) 0600 UTC 19 December; (c) 1800 UTC 19 December; (d) 0600 UTC 20 December.

cloud shield of an extratropical cyclone, was seen to the east of the Japan. During the next 12 h, the positive height anomaly over the Sea of Japan strengthened and weak negative height perturbations collocated with the cloud head of developing cyclone A (shown in Fig. 1a) were evident (Fig. 9b). Although the polar low was characterized by positive  $M_{\text{pert}}$  height perturbations, a narrow trough of low  $M_{\text{pert}}$  heights can be seen extending northward from cyclone A across Hokkaido and into the vicinity of the polar low.

The centre of the  $M_{\text{pert}}$  positive height perturbation had weakened by 1800 UTC 19 December as it slid southward across the Sea of Japan (Fig. 9c). Simultaneously, the negative  $M_{\text{pert}}$  height perturbation collocated with the cloud head of cyclone A intensified substantially while an axis of weak negative  $M_{\text{pert}}$  height perturbation extended over the polar low region. LHR was calculated using the formulation described by Cammas et al. (1994) employing  $\omega$  obtained by solving the balanced  $\omega$  equation (following Davis and Emanuel, 1991, appendix B). Calculated values of LHR (Fig. 10) are well collocated with the  $M_{\text{pert}}$  negative height perturbations at this time, confirming that the negative height perturbations are primarily attributable to positive PV produced by LHR. In the next several hours, the negative  $M_{\text{pert}}$  height perturbation continued to intensify. As the polar low moved over land, moderate precipitation occurred near the western coast of Japan (Fig. 4b). The negative height perturbation contributed by LHR reached its minimum

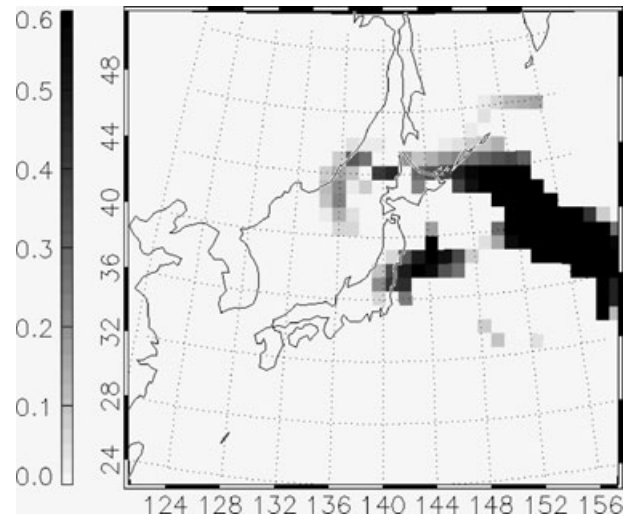


Fig. 10. The averaged LHR ( $\frac{d\theta}{dt}$ , unit:  $\text{K h}^{-1}$ ) between 650 hPa and 600 hPa are well collocated with negative height perturbations in Fig. 9c. Valid at 1800 UTC 19 December. The maximum LHR associated with the polar low was found between 650 hPa and 600 hPa.

of  $-73$  m over the polar low centre at 0200 UTC 20 December (not shown), after which time the effect of LHR associated with the polar low started to weaken. By 0600 UTC 20 December (Fig. 9d), negative height anomalies were still apparent

in the vicinity of the polar low while continued intensification of cyclone A was evident in the even more substantial negative  $M_{\text{pert}}$  heights along its developing warm front at this time.

For height perturbations associated with the  $L_{\text{pert}}$  PV anomaly (Fig. 11), positive (negative) height perturbations are associated with negative (positive) temperature anomalies. Throughout the entire analysis period, positive (negative) height perturbations dominated the western (eastern) part of the domain. Though the positive height perturbations steadily weakened over time, the negative height perturbations steadily strengthened. Also, a counter-clockwise rotation of the dipole of positive and negative height perturbations can be seen throughout this time period. At 1800 UTC 18 December (Fig. 11a), most of the Sea of Japan was dominated by a cold anomaly, though a weak negative height anomaly is hinted at over Hokkaido. By 0600 UTC 19 December (Fig. 11b), a modest negative height perturbation can be seen in the vicinity of the polar low with a strong  $L_{\text{pert}}$  height gradient to the west and southwest. During the next 12 h, although the gradient of the  $L_{\text{pert}}$  height perturbations around the polar low continued increasing, the centre of the polar low moved toward positive height perturbations (Fig. 11c). The polar low region was totally covered by positive  $L_{\text{pert}}$  height perturbations by 0600 UTC 20 December (Fig. 11d) while the gradient of the height perturbations around the polar low had also weakened significantly.

Figure 12 shows the 3 hourly evolution of the 950 hPa geopotential height change at the polar low centre during its lifecycle. The tendency and magnitude of the full inversion height changes agree well with the model data at most times except from 0000 to 0300 UTC 20 December which corresponds to the time of maximum  $M_{\text{pert}}$  contribution to development.

As shown in Fig. 12, the  $U_{\text{pert}}$  PV anomaly contributed substantially to the 950 hPa height tendency at the polar low centre during the development and dissipation of the polar low. From 0900 to 1200 UTC 19 December, the upper-level PV anomaly was the primary contributor to the development of the polar low. The positive near-surface temperature anomaly contributed secondarily while a positive height change was associated with the  $M_{\text{pert}}$  PV anomaly. From 1200 to 1800 UTC 19 December, the  $U_{\text{pert}}$  PV anomaly and the  $M_{\text{pert}}$  PV anomaly contributed nearly equally; counteracting positive height changes contributed by the  $L_{\text{pert}}$  PV anomaly from 1200 to 1500 UTC 19 December. From 1800 to 2100 UTC 19 December, there were no significant height changes contributed by the  $U_{\text{pert}}$  and  $L_{\text{pert}}$  PV anomalies while positive height perturbations were contributed by the  $M_{\text{pert}}$  PV anomaly. In the 6 h between 2100 UTC 19 December and 0300 UTC 20 December, the  $M_{\text{pert}}$  PV anomaly contributed to deepening the polar low, while the  $U_{\text{pert}}$  and  $L_{\text{pert}}$  PV anomalies contributed modest weakening. This trend was continued through 0300 to 0600 UTC 20 December during which time the

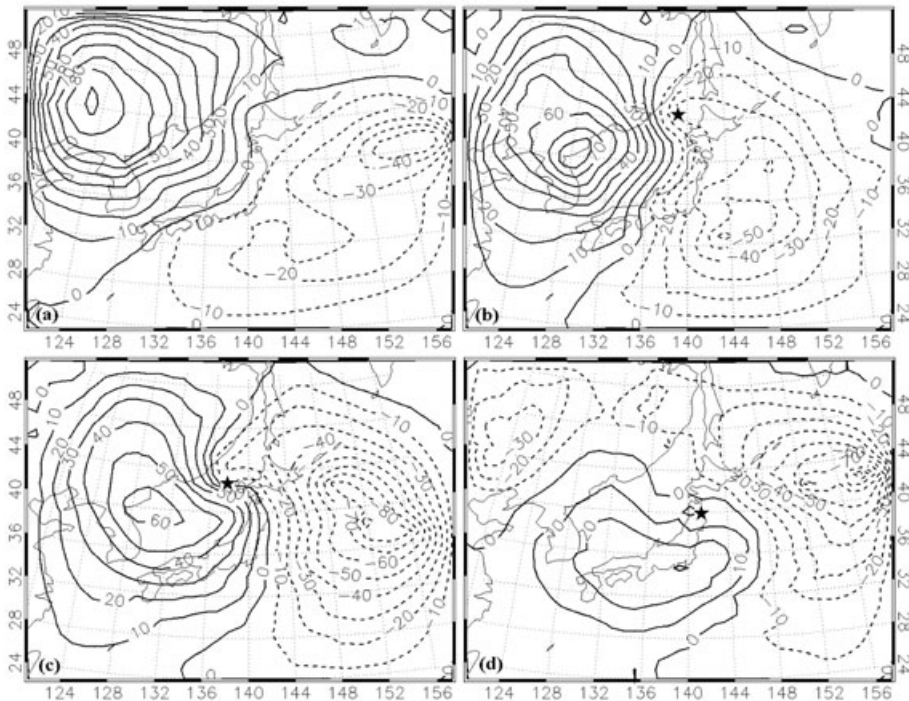


Fig. 11. The 950 hPa geopotential height perturbation associated with the  $L_{\text{pert}}$  PV anomaly. Negative (positive) geopotential height perturbations are indicated by dashed (solid) lines contoured every 10 m. The star indicates the location of the polar low centre at each time. Valid at (a) 1800 UTC 18 December; (b) 0600 UTC 19 December; (c) 1800 UTC 19 December; (d) 0600 UTC 20 December.

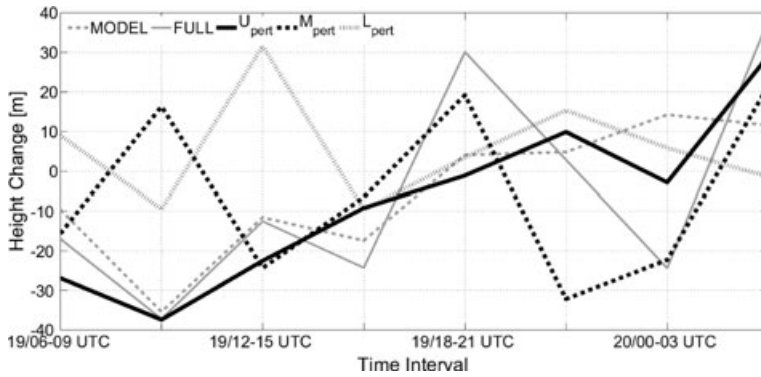


Fig. 12. The 3 hourly height changes at the 950-hPa centre of polar low: WRF outputs in grey thin dashed line; full inversions in grey thin solid line; perturbation heights associated with the  $U_{\text{pert}}$  in black thick solid line;  $M_{\text{pert}}$  in black thick dashed line;  $L_{\text{pert}}$  in black thick dotted line.

$U_{\text{pert}}$  PV anomaly made the primary contribution to decay of the polar low while the  $M_{\text{pert}}$  PV anomaly contributed secondarily.

#### 4.4. Physical factors influencing the $U_{\text{pert}}$ and $M_{\text{pert}}$ PV anomalies

As shown in the preceding section, the  $U_{\text{pert}}$  PV anomaly contributed most substantially to both the development and decay of the polar low. The effect of a tropopause-level PV anomaly on lower-tropospheric heights is dependent on the scale, magnitude and shape of the anomaly and is modulated by the intervening stratification (Hoskins et al., 1985). Figure 13 shows the PV at 350 hPa superimposed upon its associated 950-hPa  $U_{\text{pert}}$  height perturbation. The maximum PV values at 350 hPa are listed in Table 2. In the first 12 h, the maximum  $U_{\text{pert}}$  PV decreased slightly from 6.47 PVU to 6.38 PVU. Then it increased to 6.91 PVU by 1800 UTC 19 December. By 0600 UTC 20 December, the maximum  $U_{\text{pert}}$  PV had again decreased slightly to 6.74 PVU.

When a PV anomaly is more isotropic (anisotropic), the perturbation heights associated with it are more intense (weaker) (Morgan and Nielsen-Gammon, 1998; Martin and Marsili, 2002), a result of the superposition principle. The thinning and elongation of the  $U_{\text{pert}}$  PV observed from 1800 UTC 19 December to 0600 UTC 20 December (Fig. 13c and d), is the opposite of superposition and results in an increased anisotropy to the anomaly. This process was termed ‘PV attenuation’ by Martin and Marsili (2002) and it contributes to a weakening of the perturbation heights associated with the  $U_{\text{pert}}$  PV anomaly.

The largest perturbation geopotential height contributed by the  $U_{\text{pert}}$  PV anomaly was, at each time, found at 350 hPa. Thus, the ratio of the 950 to 350 hPa perturbation height in the column containing the 950 hPa perturbation height minimum can be used to assess the changes in the penetration depth of the  $U_{\text{pert}}$  PV anomaly. From Table 2, the ratio increased steadily from 0.64 at 1800 UTC 18 December to 0.81 at 0600 UTC 20 December. Coincident with these changes, the Square of Brunt–Väisälä frequency ( $N^2 = \frac{g}{\theta} \frac{d\theta}{dz}$ ) at this column decreased from  $3.73 \times 10^{-4} \text{ s}^{-2}$  to  $3.34 \times 10^{-4} \text{ s}^{-2}$  at the first 12 h and increased modestly ( $3.50 \times 10^{-4} \text{ s}^{-2}$ ) in the subsequent 12 h.

By 0600 UTC 20 December, the  $N^2$  increased substantially to  $3.77 \times 10^{-4} \text{ s}^{-2}$ .

Thus, the rapid 950 hPa  $U_{\text{pert}}$  height falls in the first 12 h of this polar low’s development were primarily a result of migration of  $U_{\text{pert}}$  PV anomaly over the ocean, where the penetration depth was increased via a reduction in the lower tropospheric static stability. At 0600 UTC 20 December, the  $U_{\text{pert}}$  perturbation height rises at 950 hPa resulted from the thinning and elongation (i.e. attenuation) of the  $U_{\text{pert}}$  PV perturbation.

As is the case in extratropical cyclones, LHR modified the environment so as to encourage development of the polar low in two ways. First, LHR in the column served to reduce the static stability. In fact, the  $N^2$  at the polar low centre gradually decreased from  $3.66 \times 10^{-4} \text{ s}^{-2}$  at 0600 UTC 19 December to  $3.59 \times 10^{-4} \text{ s}^{-2}$  at 1800 UTC 19 December, and further to  $3.43 \times 10^{-4} \text{ s}^{-2}$  at 0600 UTC 20 December. Second, as shown in Figs 9 and 10, the diabatically generated PV anomaly was associated with a negative geopotential height perturbation in the lower troposphere, which directly, though at most times secondarily, contributed to the intensification of the surface cyclone.

Based on the preceding analysis, the development processes of the polar low can be summarized as follows. Prior to the development of the polar low, a positive tropopause-level PV anomaly over the Eurasian continent, moved southeastward toward the central Sea of Japan. Near the surface, a weak positive temperature anomaly over the northern Sea of Japan (near Hokkaido) was generated by warm air advection forced by the winds associated with the  $U_{\text{pert}}$  PV anomaly. When the  $U_{\text{pert}}$  PV anomaly moved over the Sea of Japan, where the static stability was considerably lower, the negative height perturbation associated with the  $U_{\text{pert}}$  PV anomaly intensified substantially, which in turn, assisted in the intensification of the surface temperature anomaly. The combined effects of the height perturbation associated with the  $U_{\text{pert}}$  and  $L_{\text{pert}}$  PV anomalies instigated development of the polar low. This development was characterized by an outbreak of convection near the low centre. The  $M_{\text{pert}}$  PV anomaly contributed by LHR initially enhanced the development of the polar low by superposing an additional negative height perturbation in the lower troposphere. The development process of this polar low shares elements of the two stage development

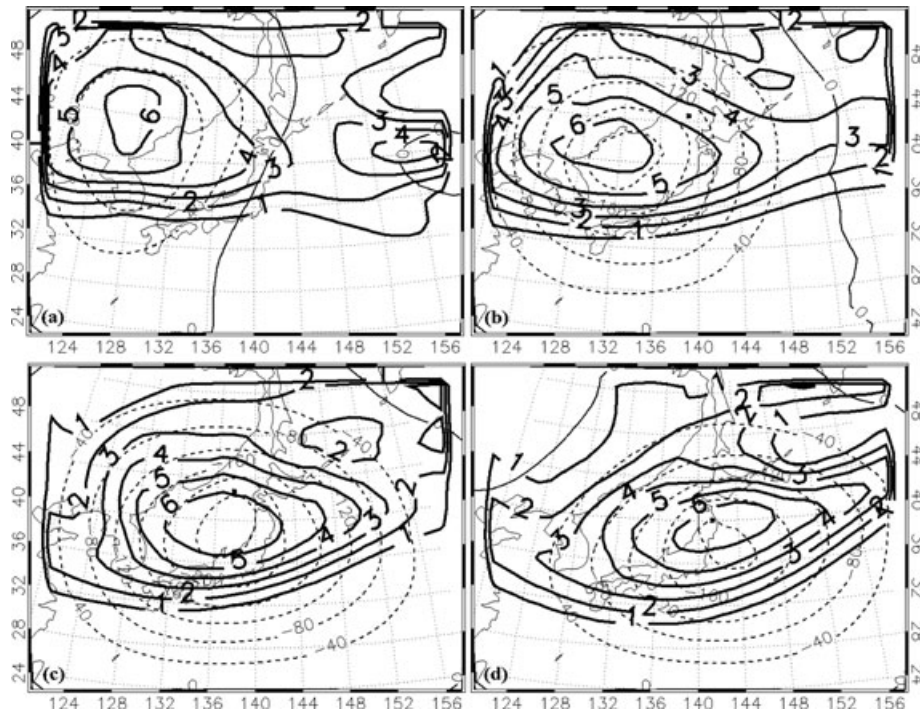


Fig. 13. As for Fig. 8 but with 350 hPa perturbation PV superimposed. Valid at (a) 1800 UTC 18 December; (b) 0600 UTC 19 December; (c) 1800 UTC 19 December; (d) 0600 UTC 20 December.

Table 2. The maximum EPV at 350 hPa; the 950-hPa and 350-hPa perturbation height associated with  $U_{\text{pert}}$ , their ratio and the corresponded square of bulk Brunt–Väisälä frequency ( $N^2$ ) at each time. The  $N^2$  is averaged from bottom to eta level 17 (eta value = 0.30, which is about 350 hPa) at the 950-hPa perturbation height minimum column.

Time	Max EPV at 350 hPa (PVU)	950 hPa (m)	350 hPa (m)	Ratio	$N^2$ ( $10^{-4} \text{ s}^{-2}$ )
1800 UTC 18 December	6.47	−119	−185	0.64	3.73
0600 UTC 19 December	6.38	−218	−315	0.69	3.34
1800 UTC 19 December	6.91	−265	−355	0.75	3.50
0600 UTC 20 December	6.74	−208	−254	0.81	3.77

proposed by Montgomery and Farrell (1992), namely the cyclogenetic influence of the  $U_{\text{pert}}$  PV anomaly and the contribution to development made by LHR. However, the analysis presented here also suggests a departure from this model in two aspects; (1) the  $U_{\text{pert}}$  PV anomaly contributed significantly during the developing and decaying stages of the polar low; (2) the dissipation of the polar low was primarily forced by the weakening of the contribution from the  $U_{\text{pert}}$  PV anomaly.

## 5. Summary and conclusion

The piecewise PV inversion method of Davis and Emanuel (1991) was used in this study to diagnose the development processes of a polar low over the Sea of Japan. It was shown that the large-scale balanced motions derived from the PV inversion show good agreement with the fully non-linear atmospheric flow. The total perturbation PV field was partitioned into three pieces

designed to isolate PV anomalies at the tropopause ( $U_{\text{pert}}$ ), those associated with mid-tropospheric PV anomalies generated by LHR ( $M_{\text{pert}}$ ), and those associated with lower boundary temperature anomalies ( $L_{\text{pert}}$ ), respectively. The piecewise PV inversion results clearly demonstrated the effect and relative importance of these discrete PV anomalies on the development of this polar low.

When the positive PV anomaly near the tropopause moved southeastward toward the Sea of Japan where the lower troposphere was less stably stratified, the effect of the upper-level positive PV anomaly on the circulation in the lower troposphere intensified. A weak positive potential temperature anomaly was generated over the northern Sea of Japan as surface cyclogenesis and associated warm air advection began to the east of Japan. As the  $U_{\text{pert}}$  PV anomaly moved over the Sea of Japan, the effect of the  $U_{\text{pert}}$  PV anomaly on lower tropospheric heights intensified significantly primarily due to a reduction of the lower

tropospheric static stability. Thus, the interaction of the  $U_{\text{pert}}$  PV anomaly and the surface warm anomaly induced the development of the polar low over the Sea of Japan.

During the development of the polar low, LHR associated with cloud and precipitation processes further reduced the static stability and, via positive perturbation PV production, superposed an additional negative height perturbation in the lower troposphere. At the same time, the effect of the  $U_{\text{pert}}$  PV anomaly made a contribution toward development equal to that produced by LHR.

When the polar low moved over land, the combined effect of the thinning and elongation of the  $U_{\text{pert}}$  PV anomaly decreased the effect of the  $U_{\text{pert}}$  PV anomaly on the lower tropospheric geopotential heights. The  $M_{\text{pert}}$  PV and  $L_{\text{pert}}$  PV anomalies also contributed to the positive geopotential height changes. As a consequence, the polar low quickly dissipated.

This study confirms that piecewise PV inversion is a useful tool for examining the dynamics of polar low formation. With this method, new insights into the effect of discrete PV anomalies on the development of polar lows can be obtained. More polar low cases, with different synoptic environments, are currently being investigated with the piecewise PV inversion method. It is hoped that the results of these analyses will add important detail to the conceptual and physical model of the development of polar lows.

## 6. Acknowledgments

The authors thank Dr. Wataru Yanase for sharing the polar low case. Thanks also to Mr. Pete Pokrandt, Mr. Yunfei Zhang, Mr. Dierk Polzin and the WRF support staff for their assistance with setting up the WRF simulations. The authors also thank Dr. Derek Posselt and Mr. Jason Otkin for assistance with the PV inversion programs. The comments from two anonymous reviewers are appreciated. The GOES-9 imagery was obtained from <http://weather.is.kochi-u.ac.jp/sat/gms.fareast/>. The precipitation data from AMeDAS radar product was obtained from JAXA/EORC. This study was supported by NASA grant NNX08AD36G.

## References

- Bracegirdle, T. J. and Gray, S. L. 2009. The dynamics of a polar low assessed using potential vorticity inversion. *Quart. J. R. Meteorol. Soc.* **135**, 880–893.
- Bresch, J. F., Reed, R. J. and Albright, M. D. 1997. A Polar-Low development over the Bering Sea: analysis, numerical simulation, and sensitivity experiments. *Mon. Wea. Rev.* **125**, 3109–3130.
- Bretherton, F. P. 1966. Baroclinic instability and the shortwave cutoff in terms of potential vorticity. *Quart. J. R. Meteorol. Soc.* **92**, 335–345.
- Cammas, J.-P., Keyser, D., Lackmann, G. and Molinari, J. 1994. Diabatic redistribution of potential vorticity accompanying the development of an outflow jet within a strong extratropical cyclones. In: *Proc. Int. Symp. on Life Cycles of Extratropical Cyclones*, Volume II, Aase Grafiske A/S, Bergen, Norway, 403–409.
- Charney, J. 1955. The use of the primitive and balance equations. *Tellus* **7**, 22–26.
- Davis, C. A. and Emanuel, K. A. 1991. Potential vorticity diagnostics of cyclogenesis. *Mon. Wea. Rev.* **119**, 1929–1953.
- Davis, C. A., Stoelinga, M. T. and Kuo, Y.-H. 1993. The integrated effect of condensation in numerical simulations of extratropical cyclogenesis. *Mon. Wea. Rev.* **121**, 2309–2330.
- Deng, A., Seaman, N. L., Hunter, G. K. and Stauffer, D. R. 2004. Evaluation of interregional transport using the MM5–SCIPUFF system. *J. Appl. Meteorol.* **43**, 1864–1886, doi: 10.1175/JAM2178.1
- Dudhia, J. 1989. Numerical study of convection observed during the winter monsoon experiment using a mesoscale two-dimensional model. *J. Atmos. Sci.* **46**, 3077–3107.
- Dudhia, J., Hong, S.-Y. and Lim, K.-S. 2008. A new method for representing mixed-phase particle fall speeds in bulk microphysics parameterizations. *J. Meteorol. Soc. Japan*, **86A**, 33–44.
- Ertel, H. 1942. Ein Neuer hydrodynamischer Wirbelsatz. *Meteorol. Z.*, **59**, 271–281.
- Grønås, S. and Kvamstø, N. G. 1995. Numerical simulations of the synoptic conditions and development of Arctic outbreak polar lows. *Tellus*, **47A**, 797–814.
- Guo, J. T., Fu, G., Li, Z. L., Shao, L. M., Duan, Y. H. and co-authors. 2007. Analyses and numerical modeling of a polar low over the Japan Sea on 19 December 2003. *Atmos. Res.*, **85**(3–4), 395–412.
- Harrold, T. W. and Browning, K. A. 1969. The polar low as a baroclinic disturbance. *Quart. J. R. Meteorol. Soc.* **95**, 710–723.
- Hong, S.-Y. and Lim, J.-O. J. 2006. The WRF single-moment 6-class microphysics scheme (WSM6). *J. Korean Meteorol. Soc.*, **42**, 129–151.
- Hong, S.-Y., Noh, Y. and Dudhia, J. 2006. A new vertical diffusion package with an explicit treatment of entrainment processes. *Mon. Wea. Rev.*, **134**, 2318–2341.
- Hoskins B. J., McIntyre, M. E. and Robertson, A. W. 1985. On the use and significance of isentropic potential vorticity maps. *Quart. J. R. Meteorol. Soc.*, **111**, 877–946.
- Kain, J. S. and Fritsch, J. M. 1990. A one-dimensional entraining/detraining plume model and its application in convective parameterization. *J. Atmos. Sci.*, **47**, 2784–2802.
- Kain, J. S. and Fritsch, J. M. 1993. Convective parameterization for mesoscale models: the Kain–Fritsch scheme. In: *The Representation of Cumulus Convection in Numerical Models*, Meteor. Monogr., No. 46, Am. Meteorol. Soc., 165–170.
- Korner, S. O. and Martin, J. E. 2000. Piecewise frontogenesis from a potential vorticity perspective: methodology and a case study. *Mon. Wea. Rev.* **128**, 1266–1288.
- Mansfield, D. A., 1974. Polar lows: the development of baroclinic disturbances in cold air outbreaks. *Quart. J. R. Meteorol. Soc.* **100**, 541–554.
- Martin, J. E. and Marsili, N. 2002. Surface cyclolysis in the North Pacific Ocean. Part II: piecewise potential vorticity diagnosis of a rapid cyclolysis event. *Mon. Wea. Rev.* **130**, 1264–1281.
- Martin, J. E. and Otkin, J. A. 2004. The rapid growth and decay of an extratropical cyclone over the central Pacific Ocean. *Wea. Forecast.* **19**, 358–376.

- Mlawer, E. J., Taubman, S. J., Brown, P. D., Iacono, M. J. and Clough, S. A. 1997. Radiative transfer for inhomogeneous atmosphere: RRTM, a validated correlated-k model for the longwave. *J. Geophys. Res.*, **102**(D14), 16663–16682.
- Montgomery, M. T. and Farrell, B. F. 1992. Polar low dynamics. *J. Atmos. Sci.*, **49**, 2484–2505.
- Morgan, M. C. and Nielsen-Gammon, J. 1998. Using tropopause maps to diagnose midlatitude weather systems. *Mon. Wea. Rev.*, **126**, 2555–2579.
- Nordeng, T. E. and Rasmussen, E. A. 1992. A most beautiful polar low. A case study of a polar low development in the Bear Island region. *Tellus*, **44A**, 81–99.
- Posselt, D. J. and Martin, J. E. 2004. The effect of latent heat release on the evolution of a warm occluded thermal structure. *Mon. Wea. Rev.*, **132**, 578–599.
- Rasmussen, E. A. 1979. Polar low as an extratropical CISK disturbance. *Quart. J. R. Meteorol. Soc.* **105**, 531–549.
- Rasmussen, E. A. and Turner, J. 2003. *Polar lows: Mesoscale Weather Systems in the Polar Regions*. Cambridge University Press, Cambridge, UK, 612 pp.
- Rasmussen, E. A., Pedersen, T. S., Pedersen, L. F. and Turner, J. 1992. Polar lows and arctic instability lows in the Bear Island region. *Tellus*, **44A**, 133–154.
- Rossby, C. G. 1940. Planetary flow patterns in the atmosphere. *Quart. J. R. Meteorol. Soc.* **66**, 68–87.
- Skamarock, W. C., Klemp, J. B., Dudhia, J., Gill, D. O., Barker, D. M. and co-authors. 2008. A description of the advanced research WRF version 3. NCAR/TN-468+STR, 126 pp.
- Stoelinga, M. T. 1996. A potential vorticity-based study of the role of diabatic heating and friction in a numerically simulated baroclinic cyclone. *Mon. Wea. Rev.*, **124**, 849–874.
- Sutcliffe, R. 1947. A contribution to the problem of development. *Quart. J. R. Meteorol. Soc.* **73**, 370–383.
- Trenberth, K. E. 1978. On the interpretation of the diagnostic quasi-geostrophic omega equation. *Mon. Wea. Rev.* **106**, 131–137.
- Wu, L. T. and Petty, G. W. 2010. Intercomparison of bulk microphysics schemes in model simulations of Polar Lows. *Mon. Wea. Rev.* **138**, 2211–2228.
- Yanase, W., Fu, G., Niino, H. and Kato, T. 2004. A Polar Low over the Japan Sea on 21 January 1997. Part II: a numerical study. *Mon. Wea. Rev.* **132**, 1552–1574.